Experimental Control of Quantum-Mechanical Entanglement in an Attosecond Pump-Probe Experiment

Lisa-Marie Koll, Laura Maikowski, Lorenz Drescher,[†] Tobias Witting, and Marc J. J. Vrakking[*]
Max-Born-Institut, Max-Born-Strasse 2A, 12x489 Berlin, Germany

(Received 2 July 2021; accepted 7 December 2021; published 24 January 2022)

Entanglement is one of the most intriguing aspects of quantum mechanics and lies at the heart of the ongoing second quantum revolution, where it is a resource that is used in quantum key distribution, quantum computing, and quantum teleportation. We report experiments demonstrating the crucial role that entanglement plays in pump-probe experiments involving ionization, which are a hallmark of the novel research field of attosecond science. We demonstrate that the degree of entanglement in a bipartite ion + photoelectron system, and, as a consequence, the degree of vibrational coherence in the ion, can be controlled by tailoring the spectral properties of the attosecond extreme ultraviolet laser pulses that are used to create them.

DOI: 10.1103/PhysRevLett.128.043201

Within the last two decades, the field of ultrafast laser spectroscopy has been enriched by the emergence of attosecond science based on the process of high-harmonic generation (HHG) [1–5]. In HHG, an atomic or molecular gas is exposed to an intense, typically infrared laser, and harmonics of the driving laser frequency are produced in a three-step process [6,7], where ionization by the intense laser field is followed by electron acceleration and electron-ion recombination accompanied by the emission of energetic photons at extreme ultraviolet (XUV) or soft x-ray wavelengths. These photons are ionizing radiation for any medium (solid, liquid, or gaseous) that is placed in its path. Thus, the production of attosecond pulses by HHG has sparked the emergence of a new research field, attosecond science, where studies of photoionization and of photoionization-induced dynamics play a prominent role.

Up to now, the possible role that ion-photoelectron entanglement plays in experimental attosecond science has not received prominent attention; nevertheless, several papers have been published that have alerted to this possibility. For example, the first application of attosecond transient absorption spectroscopy (ATAS) explored coherent hole dynamics in Kr^+ cations formed by infrared multiphoton ionization [8], and it was pointed out that in this case the electronic coherence in the cation was limited by entanglement with the accompanying photoelectron [9,10]. Extending the argument to photoionization of polyatomic molecules by attosecond pulses, the limits that entanglement imposes on the observability of attosecond charge migration was discussed in Ref. [11]. Several papers have, moreover, theoretically discussed the role of entanglement as a limiting factor to the vibrational coherence that is observable when H_2 molecules are ionized by an attosecond pulse [12,13]. A review of the possible role of quantum mechanical entanglement in atomic and molecular (AMO) physics is given in Ref. [14].

A multicomponent quantum system is entangled when it is impossible to represent its state in terms of a single product of wave functions describing the individual parts. For example, in the case of photoionization, the wave function of an entangled ion + photoelectron pair is written as a sum of such products, i.e., $\Psi \sim \sum_{\alpha,\beta} \psi_{\mathrm{ion},\alpha}\psi_{\mathrm{photoelectron},\beta}$, where α and β represent the full set of (discrete and continuous) quantum numbers needed to characterize the ionic wave function ψ_{ion} and the photoelectron wave function $\psi_{\mathrm{photoelectron}}$. Entanglement naturally arises in molecular photoionization, since the electronic and rovibrational states of the cation, and the energy and angular momentum of the photoelectron occur in different combinations and remain uncertain until they are determined by a measurement. In an entangled system, knowledge obtained about one part of the system by a measurement (or even just the possibility to perform such a measurement), has measurable consequences for what can be observed in the other part.

The entanglement that arises in photoionization limits the coherence properties of the ion and photoelectron that are produced. Here, we demonstrate this by considering the example of H_2. As previously experimentally demonstrated, photoionization of H_2 by an attosecond pulse can lead to the formation of a coherent superposition of vibrational levels in the $1s\sigma_g$ state of H_2^+ [15], corresponding to the formation of a vibrational wave packet that oscillates back and forth between the inner and outer turning point of the $1s\sigma_g$ potential energy curve. The fact that this cationic state is in a coherent superposition can be

confirmed by a pump-probe experiment, where a short near-infrared (NIR) probe pulse dissociates the molecule at a variable time delay with respect to the photoionization event, promoting the wave packet from the bound $1s\sigma_g$ to the dissociative $2p\sigma_u$ electronic state, and producing an easily measurable H^+ fragment ion.

Following a recent proposal [13], we experimentally demonstrate control of the degree of entanglement at the expense of the vibrational coherence of the H_2^+ ion, by performing pump-probe experiments where H_2 was ionized by a pair of attosecond pulses with a variable relative delay $\tau_{\mathrm{XUV-XUV}}$. In order to motivate the experiment, it is useful to consider just two of the cationic vibrational levels $H_2^+(v)$ and $H_2^+(v')$. Interference between the two attosecond pulses produces a fringe pattern in the XUV spectrum, with a fringe spacing $\Delta\omega$ that is inversely proportional to the two-pulse delay according to $\Delta\omega = 2\pi/\tau_{\mathrm{XUV-XUV}}$ (a.u.). When $\tau_{\mathrm{XUV-XUV}} = 2n\pi/\Delta E_{v,v\prime}$, where $\Delta E_{v,v'}$ is the energy separation between levels $H_2^+(v)$ and $H_2^+(v')$, and n is an integer, the photoelectron spectra accompanying the formation of $H_2^+(v)$ and $H_2^+(v')$ are shifted with respect to each other by n fringes (see Fig. 3 of Ref. [13]). If the bandwidth of the ionizing light source significantly exceeds $\Delta E_{v,v'}$, which is naturally the case for an attosecond pulse pair, the photoelectron spectra largely overlap. Then, we can approximate the ion + photoelectron wave function as $\Psi = \psi_{\mathrm{ion,v}}\psi_{\mathrm{photoelectron,v}} + \psi_{\mathrm{ion,v'}}\psi_{\mathrm{photoelectron,v'}} \approx (\psi_{\mathrm{ion,v}} + \psi_{\mathrm{ion,v'}})\psi_{\mathrm{photoelectron}}$, and the coherent superposition of cationic vibrational states $H_2^+(v)$ and $H_2^+(v')$ is observable in a pump-probe experiment, where pathways towards the final state involving $\psi_{\mathrm{ion,v}}$ and $\psi_{\mathrm{ion,v'}}$ interfere constructively or destructively as a function of pump-probe delay. Conversely, when $\tau_{\mathrm{XUV-XUV}} = (2n+1)\pi/\Delta E_{v,v'}$, then the photoelectron spectrum accompanying the formation of $H_2^+(v)$ is shifted by a half-integer number $(2n+1)/2$ fringes with respect to the photoelectron spectrum accompanying $H_2^+(v')$, implying that a possible measurement of the photoelectron kinetic energy permits to distinguish the formation of $H_2^+(v)$ and $H_2^+(v')$ with a high chance of success (see Fig. 3 of Ref. [13]). In this case, no further simplification of the entangled wave function $\Psi = \psi_{\mathrm{ion,v}}\psi_{\mathrm{photoelectron,v}} + \psi_{\mathrm{ion,v'}}\psi_{\mathrm{photoelectron,v'}}$ is possible and the ion + photoelectron entanglement is expected to limit the detection of a coherent superposition of vibrational levels $H_2^+(v)$ and $H_2^+(v')$. The criterion that $\tau_{\mathrm{XUV-XUV}} = (2n+1)\pi/\Delta E_{v,v'}$ leads to entanglement can also be derived by determining the conditions under which the off-diagonal elements of the reduced ionic density matrix, which are a measure of the vibrational coherence, vanish. As derived in the Supplemental Material [16], these matrix elements are given by

$$\rho_{vv'} \sim \int d\varepsilon F_{0,\mathrm{XUV}}(\varepsilon + E_v) F^*_{0,\mathrm{XUV}}(\varepsilon + E_{v'}) \times \cos\left[\frac{\Delta E_{v,v'}\tau_{\mathrm{XUV-XUV}}}{2}\right] \times \cos\left[\left(\frac{(E_v + E_{v'})}{2} + \varepsilon\right)\tau_{\mathrm{XUV-XUV}}\right], \quad (1)$$

where $F_{0,\mathrm{XUV}}$ is the spectral amplitude of the individual XUV pulses and ε the photoelectron energy. Hence, $\rho_{vv'}$ is zero whenever $(\Delta E_{v,v'}\tau_{\mathrm{XUV-XUV}})/2 = (2n+1)\pi/2$.

To prepare a pair of attosecond pulses with variable delay, two collinearly propagating sub-5 fs NIR pulses were produced using an ultrastable Mach-Zehnder interferometer with a motorized delay stage in one of the arms (see Fig. 1). The interferometer employed a combination of passive and active stabilization, and was constructed using optics compatible with few-cycle NIR pulses. Passive stabilization was achieved by constructing the interferometer on a vibrationally decoupled breadboard, and by mounting the retroreflecting mirror pairs on thick stainless steel plates, thus shifting the resonance frequency below prominent laboratory noise sources. This approach led to a short-term delay stability well below 10 as (1 as $= 10^{-18}$ s). Active stabilization was implemented using a frequency-stable, 473 nm cw laser that copropagated in both interferometer arms, with a 30 arcmin wedge inserted into one of the two arms to induce tilt fringes in the plane of detection. Path length variations were measured by Fast Fourier transform (FFT) processing of fringe patterns recorded by a fast USB3 CMOS camera, using the Takeda algorithm [17], and were used to derive an error signal that was fed into a proportional-integral-derivative (PID) controller used to drive the delay stage. Thus, two-pulse delay fluctuations could be kept below 10 as rms for multiple days while scanning $\tau_{\mathrm{XUV-XUV}}$ over a range >100 fs.

The NIR pulse pair was used to generate high harmonics in Ar, within an attosecond pump-probe setup that has been previously described [18,19] (see Supplemental Material [16] for a concise summary). Two-pulse delays $\tau_{\mathrm{XUV-XUV}}$ between 11 and 102 fs (in steps of 3 fs) were employed, with the lower limit chosen to avoid optical interferences between the two NIR pulses. Inspection of the HHG spectra recorded under these conditions (see Fig. 1) revealed clear delay-dependent spectral modulations with a fringe spacing inversely proportional to $\tau_{\mathrm{XUV-XUV}}$, demonstrating that the HHG by the 2nd NIR pulse was not appreciably affected by modifications of the generating medium by the 1st NIR pulse. The XUV pulses were collinearly overlapped with a co-polarized replica of the NIR pulse, and focused into a velocity map imaging (VMI) spectrometer [20], where both pulses crossed a pulsed H_2 jet generated within the repeller

electrode [21]. H^+ ions resulting from two-color XUV + NIR dissociative ionization were projected onto a 2D MCP + phosphor screen detector, and recorded using a CCD camera. The XUV and NIR polarizations were in the plane of the MCP detector, permitting use of an inverse Abel transform (see Supplemental Material [16]) to retrieve the three-dimensional (3D) H^+ momentum distributions. Images were recorded as a function of $\tau_{\mathrm{XUV-XUV}}$, and as a function of the XUV-NIR time delay $\tau_{\mathrm{XUV-NIR}}$, which was varied between −50 and +800 fs in steps of 4 fs. For each $\tau_{\mathrm{XUV-XUV}}$ and $\tau_{\mathrm{XUV-NIR}}$, up to 8 pump-probe scans were performed, where data was collected for 2000 laser shots at each delay.

An example of a measured and an inverted image are shown in Fig. 1. They show that the H^+ momentum distribution consists of a contribution at low momentum resulting from single photon XUV dissociative ionization (where the dissociation into $H^+ + H$ takes place on the $1s\sigma_g$ potential energy curve) and a contribution at higher momentum resulting from $1 + 1'$ XUV + NIR two-color dissociative ionization (where the dissociation takes place on the $2p\sigma_u$ potential energy curve). The former signal was used for normalization purposes, since it is linearly proportional to both the XUV flux and the H_2 gas density.

Considering that the 3D H^+ momentum distributions retrieved by Abel inversion only depend on the absolute H^+ velocity v_{H^+}, and the angle θ between this velocity and the XUV and NIR polarization axis, the experiment led to the determination of a 4D probability distribution $P(v_{H^+}, \cos\theta, \tau_{\mathrm{XUV-XUV}}, \tau_{\mathrm{XUV-NIR}})$. Since the XUV + NIR dissociative ionization is a two-photon process, this probability distribution can be written as

$$\begin{aligned} P(v_{H^+}, \cos\theta, \tau_{\mathrm{XUV-XUV}}, \tau_{\mathrm{XUV-NIR}}) &= \beta_0(v_{H^+}, \tau_{\mathrm{XUV-XUV}}, \tau_{\mathrm{XUV-NIR}}) \\ &\times \{1 + \beta_2(v_{H^+}, \tau_{\mathrm{XUV-XUV}}, \tau_{\mathrm{XUV-NIR}}) P_2(\cos\theta) \\ &+ \beta_4(v_{H^+}, \tau_{\mathrm{XUV-XUV}}, \tau_{\mathrm{XUV-NIR}}) P_4(\cos\theta)\}, \end{aligned} \tag{2}$$

where $P_2(\cos\theta)$ and $P_4(\cos\theta)$ are 2nd order and 4th order Legendre polynomials [22]. Figures 2(a)–2(f) show experimental results for $\beta_0(v_{H^+}, \tau_{\mathrm{XUV-XUV}}, \tau_{\mathrm{XUV-NIR}})$,

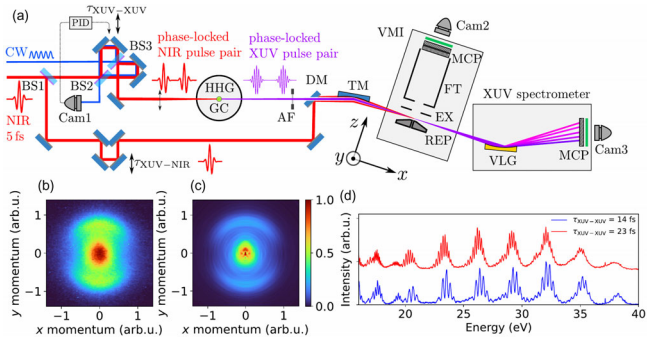

FIG. 1. Setup for measuring the influence of quantum mechanical entanglement on vibrational wave packet dynamics in H_2^+. (a) Neutral H_2 molecules injected into the apparatus through a nozzle incorporated in the repeller (REP) of the velocity map imaging (VMI) spectrometer, are dissociatively ionized using a two-color XUV + NIR laser field, where the XUV field consists of a two-pulse pair with a relative delay $\tau_{\mathrm{XUV-XUV}}$, which is followed by the NIR pulse after a delay $\tau_{\mathrm{XUV-NIR}}$. The XUV pulse pair is generated by passing ultrashort NIR pulses through a passively and actively stabilized Mach-Zehnder interferometer prior to their use within a high-harmonic generation gas cell (GC). The XUV and NIR pulses are collinearly combined using a drilled mirror (DM) and focused using a toroidal mirror (TM). The two-pulse XUV spectrum is monitored using an XUV spectrometer. Abbreviations: beam splitters (BS1-BS3); proportional-integral-derivative (PID) feedback for stabilization of $\tau_{\mathrm{XUV-XUV}}$; cameras (Cam1-3); aluminum filter (AF); Extractor electrode (EX); flight tube (FT); microchannel plate (MCP); variable line-space grating (VLG); (b) and (c) typical example of a raw H^+ VMI image and a slice through the 3D momentum distribution obtained via Abel inversion; (d) XUV spectrum recorded for two delays $\tau_{\mathrm{XUV-XUV}}$, revealing fringes in the XUV spectrum resulting from the interference between the two XUV pulses.

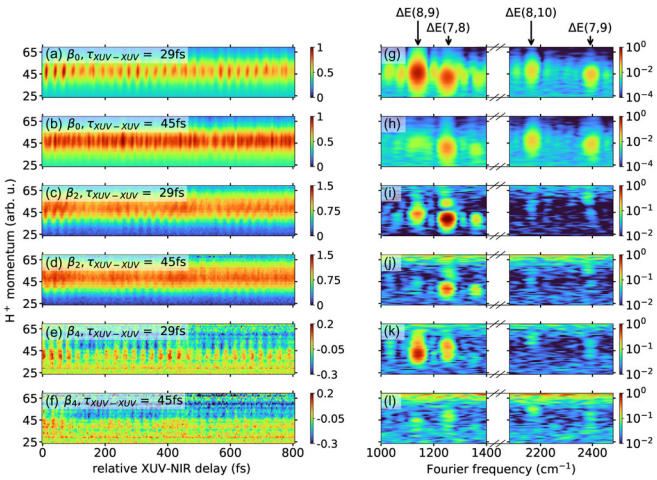

FIG. 2. Experimentally observed wave packet dynamics following ionization of H_2 by a pair of XUV pulses separated by $\tau_{\mathrm{XUV-XUV}} = 29$ and 45 fs: (a)–(f) $\beta_0(v_{H^+}, \tau_{\mathrm{XUV-XUV}}, \tau_{\mathrm{XUV-NIR}})$, $\beta_2(v_{H^+}, \tau_{\mathrm{XUV-XUV}}, \tau_{\mathrm{XUV-NIR}})$, and $\beta_4(v_{H^+}, \tau_{\mathrm{XUV-XUV}}, \tau_{\mathrm{XUV-NIR}})$ obtained by Abel inversion of the experimental VMI images. The vertical axis is given in pixel units of the CCD camera used in the VMI spectrometer, and represents the H^+ velocity in arbitrary units; (g)–(l) Fourier transform power spectra $\mathrm{FTPS}(v_{H^+}, \tau_{\mathrm{XUV-XUV}}, \omega)$ of $\beta_0(v_{H^+}, \tau_{\mathrm{XUV-XUV}}, \tau_{\mathrm{XUV-NIR}})$, $\beta_2(v_{H^+}, \tau_{\mathrm{XUV-XUV}}, \tau_{\mathrm{XUV-NIR}})$, and $\beta_4(v_{H^+}, \tau_{\mathrm{XUV-XUV}}, \tau_{\mathrm{XUV-NIR}})$, obtained by a Fast fourier transform. The vertical axis coincides with the vertical axis in (a)–(f), whereas the horizontal axis gives the Fourier frequency in cm^{-1}, permitting a straightforward assignment to two-level quantum beats and a comparison with available literature values (see Table I). Importantly, the intensity of the nearest-neighbor quantum beats in the FTPS are significantly different for the two different values of $\tau_{\mathrm{XUV-XUV}}$.

TABLE I. Comparison of experimental Fourier frequencies with literature values. Column 2 was obtained by performing a statistical analysis for the measured FTPS$(v_{H^+}, \tau_{XUV-XUV}, \omega)$ after integrating over v_{H^+}, using the data for β_0 only (see Fig. 2). Column 3 was obtained by fitting the peak intensities in the FTPS as a function of $\tau_{XUV-XUV}$ to a sinusoidal curve (see Fig. 3).

Fourier peak (Fig. 1)	Fourier frequency obtained by FFT of pump-probe delay scans (cm^{-1}) (see Fig. 2)	Fourier frequency obtained by FFT of the $\tau_{XUV-XUV}$ delay dependence of the FTPS (cm^{-1}) (see Fig. 3)	Assignment (v, v')	Literature value (cm^{-1}) [a]
A	1138 ± 7	1141 ± 7	(8,9)	1130.1
B	1252 ± 7	1259 ± 6	(7,8)	1262.5
C	2168 ± 16	2167 ± 11	(8,10)	2127.8
D	2396 ± 17	2387 ± 13	(7,9)	2392.6

[a]Following Ref. [23].

$\beta_2(v_{H^+}, \tau_{XUV-XUV}, \tau_{XUV-NIR})$, and $\beta_4(v_{H^+}, \tau_{XUV-XUV}, \tau_{XUV-NIR})$ as a function of v_{H^+} and $\tau_{XUV-NIR}$ for two different values $\tau_{XUV-XUV} = 29$ and 45 fs. The measurements show wave packet motion with a vibrational period of almost 30 fs, and reveal the dephasing and rephasing that is commonly observed when coherent superpositions consisting of ≥ 3 states are excited. A profitable way to analyze these results is by performing a Fourier transform over $\tau_{XUV-NIR}$, and plotting the Fourier transform power spectrum FTPS $(v_{H^+}, \tau_{XUV-XUV}, \omega)$, where ω is the Fourier frequency. FTPSs for the data shown in Figs. 2(a)–2(f) are presented in Figs. 2(g)–2(l). They reveal that the observed dependence of $\beta_0(v_{H^+}, \tau_{XUV-XUV}, \tau_{XUV-NIR})$, $\beta_2(v_{H^+}, \tau_{XUV-XUV}, \tau_{XUV-NIR})$, and $\beta_4(v_{H^+}, \tau_{XUV-XUV}, \tau_{XUV-NIR})$ on $\tau_{XUV-NIR}$ is determined by a number of nearest-neighbor and next-nearest-neighbor quantum beats. Column 2 of Table I presents an overview of the most prominent beat frequencies that are observable in Fig. 2, which can readily be assigned using available spectroscopic information (last column) [23]. Importantly, whereas the contributions of next-nearest neighbor quantum beats are of comparable strength for $\tau_{XUV-XUV} = 29$ and 45 fs, the nearest-neighbor quantum beats are much more prominent in the former measurement, and only weakly visible in the latter.

For each $\tau_{XUV-XUV}$ between 11 and 102 fs, a scan like the one shown in Fig. 2 was performed, allowing a determination of the intensity of the nearest-neighbor and next-nearest neighbor quantum beats as a function of $\tau_{XUV-XUV}$. This intensity dependence is shown in Fig. 3, and represents the main result of our work. Figure 3 shows that the intensity of each two-level quantum beat in the FTPS oscillates as a function of $\tau_{XUV-XUV}$ with a period (see figure) inversely proportional to the frequency of the quantum beat. Thus, Fig. 3 provides experimental confirmation that vibrational quantum beats are observable when $\tau_{XUV-XUV} = 2n\pi/\Delta E_{v,v'}$ and are absent or only weakly observable when $\tau_{XUV-XUV} = (2n+1)\pi/\Delta E_{v,v'}$, with n an integer. Values of $\Delta E_{v,v'}$ extracted from the fits shown in Fig. 3 by means of a weighted averaging are shown in the 3rd column of Table I. As before, they show reasonable agreement with literature results.

The behavior in Fig. 3 is caused by quantum mechanical entanglement of the H_2^+ ion with the photoelectron that

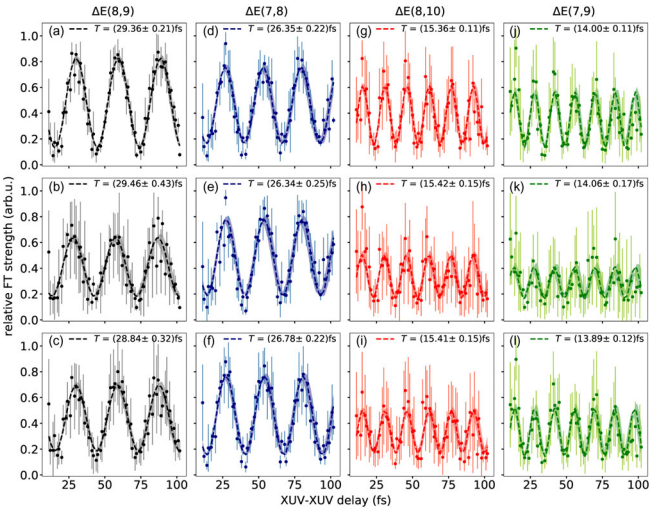

FIG. 3. Intensities of peaks in the Fourier transform power spectrum FTPS$(v_{H^+}, \tau_{XUV-XUV}, \omega)$ as a function of two-pulse delay $\tau_{XUV-XUV}$, for 4 selected values of the Fourier frequency: (a)–(c) FTPS$_{\beta_0}(v_{H^+}, \tau_{XUV-XUV}, \omega)$, FTPS$_{\beta_2}(v_{H^+}, \tau_{XUV-XUV}, \omega)$, and FTPS$_{\beta_4}(v_{H^+}, \tau_{XUV-XUV}, \omega)$ with ω corresponding to the energy difference between $v^+ = 8$ and 9; (d)–(f) the same, with ω corresponding to the energy difference between $v^+ = 7$ and 8; (g)–(i), the same, with ω corresponding to the energy difference between $v^+ = 8$ and 10; (j)–(l) the same, with ω corresponding to the energy difference between $v^+ = 7$ and 9. The oscillations in the FTPS (experimental data points given by symbols) are fitted to sinusoidal curves (dashed lines, with shaded area according to the standard deviation of the fit parameters), leading to a determination of the oscillation periods shown at the top of each figure. The oscillation periods obtained for FTPS$_{\beta_0}(v_{H^+}, \tau_{XUV-XUV}, \omega)$, FTPS$_{\beta_2}(v_{H^+}, \tau_{XUV-XUV}, \omega)$, and FTPS$_{\beta_4}(v_{H^+}, \tau_{XUV-XUV}, \omega)$ are combined to obtain values that are compared to available spectroscopic data in column 3 of Table I.

accompanies its formation. Although we have focused our attention on the vibrational coherence in the H_2^+ ion within the pump-probe experiment, this ion remains part of an entangled system throughout the experiment. Modifying the spectral properties of the attosecond XUV pulse pair modifies the photoelectron spectra accompanying the different H_2^+ vibrational states, and thus affects the degree of ion + photoelectron entanglement, thereby controlling the observability of the H_2^+ vibrational coherences.

It should be acknowledged and emphasized that the use of a two-pulse sequence to tailor excited state properties is nothing new [24]. This approach underlies Ramsey-type Fourier transform spectroscopy [25], has been exploited in coherent control experiments [26], and plays an essential role in applications ranging from multidimensional spectroscopy [27] to hyperspectral imaging [28,29]. The unique aspect of our experiment is that the two-pulse sequence is not used to control excited state populations, but is used to control the entanglement in a bipartite system consisting of an ion and a photoelectron. Given that these states are formed by an ionization process, rather than a resonant bound-to-bound transition, the cationic vibrational state populations do not depend at all on the two-pulse delay [13], and, except for the narrow fringe patterns caused by $\tau_{\mathrm{XUV-XUV}}$, the same is true for the photoelectron spectrum that accompanies the ionization process. What radically changes as a function of $\tau_{\mathrm{XUV-XUV}}$ is the ion + photoelectron entanglement. This entanglement determines the observability of quantum beats between pairs of vibrational states within the pump-probe experiment. Whenever the photoelectron spectrum accompanying both vibrational states is very similar (i.e., offset by an integer number of fringes in the XUV spectrum), the experiment reveals pronounced quantum beats, whereas these quantum beats are greatly suppressed when the XUV fringe pattern produces a situation where the photoelectron spectrum accompanying both vibrational states under consideration is different.

Ion + photoelectron entanglement is a so far underappreciated aspect of pump-probe experiments involving ionization, which are ubiquitous in attosecond science. Indeed, it may be expected that ion + photoelectron entanglement is highly common within attosecond science. As an example, we mention our previous work on laboratory frame electron localization in H_2 [30], which was a first example of attosecond pump-probe spectroscopy to molecules, and which can be described within a very similar conceptual framework as the work presented here. Electron localization in the dissociation of H_2^+ into $H^+ + H$ requires that the parity of the ionic wave function is broken, i.e., that the ion is produced in a coherent superposition of gerade and ungerade states. However, photoionization produces the H_2^+ ion as part of a bipartite entangled state, where formation of gerade ionic states is accompanied by the emission of an "ungerade" photoelectron with odd orbital angular momentum, and formation of ungerade ionic states is accompanied by the emission of a "gerade" photoelectron with even angular momentum. The ionic coherence that is needed to observe laboratory frame electron localization is absent in this entangled state and can be induced within a pump-probe experiment when interactions of the ion or the photoelectron with the probe laser reduce the degree of entanglement. Indeed, both mechanisms were observed in Ref. [30].

Our work represents both a warning and an opportunity. It is a warning, because it demonstrates how ion + photoelectron entanglement may prevent the observation of coherent dynamics in ions or photoelectrons, which is the objective of many attosecond experiments. It is also an opportunity, because it shows that tailoring the properties of the attosecond laser pulses can be used to emphasize the role of selected two-level quantum beats. This may be of particular interest in current efforts targeting the observation of attosecond to few-femtosecond charge migration and charge-directed reactivity [31,32], where initial experimental results have suggested the key role of particular two-level quantum beats [33]. Finally, our work draws attention to the links that may be established between ultrafast laser spectroscopy and the field of quantum information [14], where the experimental tools of attosecond science may create hitherto unsuspected opportunities.

*Corresponding author.
marc.vrakking@mbi-berlin.de
†Present address: Department of Chemistry, University of California, Berkeley, California 94720, USA.

[1] F. Krausz and M. Ivanov, Attosecond physics, Rev. Mod. Phys. **81**, 163 (2009).
[2] F. Lepine, M. Y. Ivanov, and M. J. J. Vrakking, Attosecond molecular dynamics: Fact or fiction? Nat. Photonics **8**, 195 (2014).
[3] K. Ramasesha, S. R. Leone, and D. M. Neumark, Real-time probing of electron dynamics using attosecond time-resolved spectroscopy, in *Annual Review of Physical Chemistry*, edited by M. A. Johnson and T. J. Martinez (Annual Reviews, Palo Alto, 2016), Vol. 67, pp. 41–63, https://doi.org/10.1146/annurev-physchem-040215-112025.
[4] M. Nisoli *et al.*, Attosecond electron dynamics in molecules, Chem. Rev. **117**, 10760 (2017).
[5] J. Biegert *et al.*, Attosecond technology(ies) and science, J. Phys. B **54**, 070201 (2021).
[6] K. J. Schafer, B. Yang, L. F. DiMauro, and K. C. Kulander, Above Threshold Ionization Beyond the High Harmonic Cutoff, Phys. Rev. Lett. **70**, 1599 (1993).
[7] P. B. Corkum, Plasma Perspective on Strong-Field Multiphoton Ionization, Phys. Rev. Lett. **71**, 1994 (1993).
[8] E. Goulielmakis *et al.*, Real-time observation of valence electron motion, Nature (London) **466**, 739 (2010).
[9] S. Pabst *et al.*, Decoherence in Attosecond Photoionization, Phys. Rev. Lett. **106**, 053003 (2011).

[10] O. Smirnova, Spectroscopy: Attosecond prints of electrons, Nature (London) **466**, 701 (2010).
[11] M. Ruberti, Onset of ionic coherence and ultrafast charge dynamics in attosecond molecular ionization, Phys. Chem. Chem. Phys. **21**, 17584 (2019).
[12] T. Nishi, E. Lötstedt, and K. Yamanouchi, Entanglement and coherence in photoionization of H2 by an ultrashort XUV laser pulse, Phys. Rev. A **100**, 013421 (2019).
[13] M. J. J. Vrakking, Control of Attosecond Entanglement and Coherence, Phys. Rev. Lett. **126**, 113203 (2021).
[14] M. C. Tichy, F. Mintert, and A. Buchleitner, Essential entanglement for atomic and molecular physics, J. Phys. B **44**, 192001 (2011).
[15] F. Kelkensberg, C. Lefebvre, W. Siu, O. Ghafur, and T. T. Nguyen-Dang, Molecular Dissociative Ionization and Wave-Packet Dynamics Studied Using Two-Color XUV and IR Pump-Probe Spectroscopy, Phys. Rev. Lett. **103**, 123005 (2009).
[16] See Supplemental Material at http://link.aps.org/supplemental/10.1103/PhysRevLett.128.043201 for a description of the Attosecond Setup, the Legendre polynomial-based Abel Inversion routine, and a derivation of Eq. (1).
[17] M. Takeda, H. Ina, and S. Kobayashi, Fourier-transform method of fringe-pattern analysis for computer-based topography and interferometry, J. Opt. Soc. Am. **72**, 156 (1982).
[18] C. Neidel *et al.*, Probing Time-Dependent Molecular Dipoles on the Attosecond Time Scale, Phys. Rev. Lett. **111**, 033001 (2013).
[19] L. Drescher *et al.*, Extreme-ultraviolet spectral compression by four-wave mixing, Nat. Photonics **15**, 263 (2021).
[20] A. T. J. B. Eppink and D. H. Parker, Velocity map imaging of ions and electrons using electrostatic lenses: Application in photoelectron and photofragment ion imaging of molecular oxygen, Rev. Sci. Instrum. **68**, 3477 (1997).
[21] O. Ghafur *et al.*, A velocity map imaging detector with an integrated gas injection system, Rev. Sci. Instrum. **80**, 033110 (2009).
[22] R. K. Sander and K. R. Wilson, Double absorption photofragment spectroscopy: A new tool for probing unimolecular processes, J. Chem. Phys. **63**, 4242 (1975).
[23] K. P. Huber and G. Herzberg, Constants of diatomic molecules, in *Molecular Spectra and Molecular Structure: IV. Constants of Diatomic Molecules*, edited by K. P. Huber and G. Herzberg (Springer US, Boston, MA 1979), p. 8–689, https://doi.org/10.1007/978-1-4757-0961-2_2.
[24] N. F. Scherer *et al.*, Fluorescence-detected wave packet interferometry: Time resolved molecular spectroscopy with sequences of femtosecond phase-locked pulses, J. Chem. Phys. **95**, 1487 (1991).
[25] J. Morgenweg, I. Barmes, and K. S. E. Eikema, Ramsey-comb spectroscopy with intense ultrashort laser pulses, Nat. Phys. **10**, 30 (2014).
[26] H. Katsuki, H. Chiba, C. Meier, B. Girard, and K. Ohmori, Actively Tailored Spatiotemporal Images of Quantum Interference on the Picometer and Femtosecond Scales, Phys. Rev. Lett. **102**, 103602 (2009).
[27] M. C. Asplund, M. T. Zanni, and R. M. Hochstrasser, Two-dimensional infrared spectroscopy of peptides by phase-controlled femtosecond vibrational photon echoes, Proc. Natl. Acad. Sci. U.S.A. **97**, 8219 (2000).
[28] S. Witte *et al.*, Lensless diffractive imaging with ultra-broadband table–top sources: From infrared to extreme-ultraviolet wavelengths, Light-Sci. Appl. **3**, e163 (2014).
[29] A. Perri *et al.*, Hyperspectral imaging with a TWINS birefringent interferometer, Opt. Exp. **27**, 15956 (2019).
[30] G. Sansone *et al.*, Electron localization following attosecond molecular photoionization, Nature (London) **465**, 763 (2010).
[31] F. Remacle and R. D. Levine, An electronic time scale in chemistry, Proc. Natl. Acad. Sci. U.S.A. **103**, 6793 (2006).
[32] J. Breidbach and L. S. Cederbaum, Migration of holes: Formalism, mechanisms, and illustrative applications, J. Chem. Phys. **118**, 3983 (2003).
[33] F. Calegari *et al.*, Ultrafast electron dynamics in phenylalanine initiated by attosecond pulses, Science **346**, 336 (2014).